

The interplay between anisotropy and strain localisation in granular soils: a multiscale insight

J. ZHAO* and N. GUO*

This paper presents a multiscale investigation on the interplay among inherent anisotropy, fabric evolution and strain localisation in granular soils, based on a hierarchical multiscale framework with rigorous coupling of the finite-element method (FEM) and discrete-element method (DEM). DEM assemblies with elongated particles are generated to simulate inherent anisotropy and are embedded to the Gauss points of the FEM mesh to derive the required constitutive relation. Specimens prepared with different bedding plane angles are subjected to biaxial shear under either smooth or rough loading platens. Key factors and physical mechanisms contributing towards the occurrence and development of strain localisation are examined. The competing evolutions of two sources of anisotropy, one related to particle orientations and the other related to contact normals, are found to underpin the development of the shear band. A single band pattern is observed under smooth boundary conditions, and its orientation relative to the bedding plane depends critically on the relative dominance between the two anisotropies. Under rough boundary conditions, the non-coaxial material response and the boundary constraint jointly lead to cross-shaped double shear bands. The multiscale simulations indicate that the DEM assemblies inside the shear band(s) undergo extensive shearing, fabric evolution and particle rotation, and may reach the critical state, while those located outside the shear band(s) experience mild loading followed by unloading. The particle-orientation-based fabric anisotropy needs significantly larger shear and dilation for mobilisation than the contact-normal based one. The asynchrony in evolution of the two fabric anisotropies can cause non-coaxial responses for initially coaxial packings, which directly triggers strain localisation.

KEYWORDS: anisotropy; discrete-element modelling; finite-element modelling; numerical modelling; strain localisation

INTRODUCTION

Many intriguing phenomena observed in granular media reflect non-trivial microstructural mechanisms that can be better understood from a multiscale perspective (Guo & Zhao, 2014). Strain localisation and anisotropy are among the representative ones. Strain localisation in sand is widely regarded as an important precursor associated with the failure of geomaterials and relevant geostructures, while anisotropy underpins key mechanical responses of granular media including strength, deformation and failure. As most in-situ granular soils are naturally inherently anisotropic, how anisotropy interplays with strain localisation during the inception and formation of the latter has drawn sustained attention. Anisotropy has indeed been found among the key factors, along with density, boundary conditions, drainage conditions and specimen dimensions, affecting the occurrence of strain localisation in granular soils (Vardoulakis, 1996; Mokni & Desrues, 1999; Desrues & Viggiani, 2004; Rechenmacher, 2006). Experimental studies by Tatsuoka *et al.* (1990) and Lade *et al.* (2008) showed that the initiation and development of a shear band in sand can be greatly influenced by the presence of anisotropy.

Numerous past studies, including those dealing with the effect of anisotropy, have treated strain localisation as a

material instability based on bifurcation analysis (Rudnicki & Rice, 1975; Bigoni & Loret, 1999, among others). There have been attempts to simulate the phenomenon of strain localisation in anisotropic sand samples, based on either continuum modelling, typically by finite-element method (FEM), or micromechanics using the discrete-element method (DEM) (Bauer *et al.*, 2004; Tejchman & Górski, 2010; Fu & Dafalias, 2011b). Despite being successful in reproducing important aspects of strain localisation, such as the correlation between shear band pattern and inclination and inherent anisotropy, these studies are not without limitations. DEM-based micromechanics approaches, for example, typically have difficulties in handling the large number of particles required to simulate a real engineering problem. Continuum modelling often relies on constitutive relations which are phenomenological in nature. To trigger strain localisation, it is common to introduce imperfections in elements or random field distribution of material properties in a FEM simulation, which may add subjectivity and uncertainties to the simulations and distract from the identification of key mechanisms of strain localisation. There is another popular class of micromechanics approach pioneered by Chang and co-workers, which has been applied to treat inherent anisotropy and instability in sand (Chang & Hicher, 2005; Hicher *et al.*, 2008; Chang & Yin, 2010; Chang *et al.*, 2011). Notably, most studies have neglected the evolution of fabric anisotropy and how it interacts with the developing shear band. Indeed, anisotropy may evolve during the loading process, especially in regions where strain is localised. It is evident that an evolving fabric may affect importantly the development of the shear band as well as its final pattern (Gao & Zhao, 2013). To quantify the essential feature of fabric and its evolution, a

Manuscript received 18 September 2014; revised manuscript accepted 15 April 2015.

Discussion on this paper closes on 1 January 2016, for further details see p. ii.

* Department of Civil and Environmental Engineering, Hong Kong University of Science and Technology, Clearwater Bay, Kowloon, Hong Kong.

micromechanics approach has been proved more appropriate (Guo & Zhao, 2013b; Zhao & Guo, 2013), whereas a continuum approach may be more efficient and straightforward to simulate strain localisation as a boundary value problem (BVP). To capture the interplay between the two, a combination of the two approaches is desirable.

In this study, the authors employ a hierarchical multiscale approach coupling DEM and FEM (Guo & Zhao, 2013a, 2014) to model the behaviour of anisotropy, fabric evolution and strain localisation in a granular soil. The multiscale framework is in line with early studies by Nitka *et al.* (2011) and Andrade *et al.* (2011). Specifically, the multiscale approach treats a continuum domain by FEM and embeds a DEM assembly as the representative volume element (RVE) at each FEM Gauss point to derive the material constitutive relation. It helps to circumvent the phenomenological assumptions and parameter fitting in conventional continuum approaches, expedites a direct link of macroscopic soil behaviour with its microscopic origin and enables micromechanical insights to be gained into complex soil properties such as history dependency, non-coaxiality, dilatancy and critical state (Schofield & Wroth, 1968; Gutierrez & Ishihara, 2000; Yu & Yuan, 2006; Tejchman & Wu, 2009; Mühlhaus *et al.*, 2010), as well as the anisotropy and strain localisation to be considered here.

APPROACH AND FORMULATION

The hierarchical multiscale framework is based on a rigorous coupling of two open-source codes – Escript (FEM engine, Gross *et al.*, 2007) and Yade (DEM engine, Šmilauer *et al.*, 2010), which is briefly summarised below. A detailed formulation and solution procedure of the scheme can be found in Guo & Zhao (2014).

Governing equation and the FEM model

The governing equation of a BVP can be written in the following strong form (considering quasi-static equilibrium in the absence of gravity)

$$\sigma_{ij,j} = 0 \quad (1)$$

where σ_{ij} is the stress tensor. The FEM commonly employs a variational weak form of equation (1), which is transformed into a system of linear equations upon discretisation

$$\mathbf{K}\mathbf{u} = \mathbf{f} \quad (2)$$

where \mathbf{K} is the tangent stiffness matrix, \mathbf{u} is the FEM nodal displacement vector, and \mathbf{f} is the nodal force lumped from the applied boundary traction.

A conventional FEM needs to assume an elasto-plastic (or hypoplastic) relation to describe the material response and to assemble \mathbf{K} from the elasto-plastic modulus \mathbf{D}^{ep} which is highly non-linear and history-dependent for granular soils. The hierarchical multiscale approach abandons any assumption of phenomenological constitutive models, and incurs separate DEM simulations at each FEM Gauss point to provide the material constitutive responses. For a given global loading step, the typical solution procedure of the multiscale approach consists of the following substeps: (a) evaluating the tangent modulus D_{ijkl} based on the DEM packing at each Gauss point to form \mathbf{K} ; (b) interpolating the local deformation $u_{i,j}$ at each Gauss point from the (trial) FEM solution and applying them as boundary conditions for the corresponding RVE packing; (c) solving the local RVE, updating the total stress at the Gauss point, and assembling the global tangent operator and stress tensor for the FEM domain; (d) performing Newton–Raphson iteration over

(a) to (c) to find a converged solution of equation (2) for the displacement field \mathbf{u} .

DEM model and macroscopic definitions

To simulate inherent anisotropy, the present authors have modified the DEM model in Guo & Zhao (2014) by replacing the circular particles therein with elongated clumps consisting of two identical discs, as shown in Fig. 1 (see also Evans & Frost, 2010; Li & Yu, 2010). The centroid distance of the two clumped circular discs is set to be $1.25r$ (r = radius of the constituent discs), which leads to an aspect ratio of 1.625. The area A_{cl} , the equivalent radius r_{eq} and the inertia of moment (with regard to the mass centre) I_{cl} of the clump can be computed as follows

$$\begin{cases} A_{\text{cl}} = 2 \left[\sqrt{1 - 0.625^2} \times 0.625 + \pi - \arccos(0.625) \right] \\ \quad \times r^2 \approx 5.4676r^2 \\ r_{\text{eq}} := \sqrt{A_{\text{cl}}/\pi} \approx 1.3192r \\ I_{\text{cl}} \approx 0.9994 \times m_{\text{cl}}r^2 \end{cases} \quad (3)$$

where m_{cl} is the mass of the clump. I_{cl} in equation (3) is estimated by discretising the clump boundary to a star-shaped polygon (see Fig. 1). The coefficient is determined by approximating the clump boundary with a 3000-segment polygon (this leads to an accuracy up to four decimal places).

A similar linear force–displacement contact law for the DEM model as described in Guo & Zhao (2014) is followed, adopting a normal stiffness $k_n/r_{\text{eq}}^* = 455$ MPa and a tangential stiffness $k_t = 0.3 k_n$, where r_{eq}^* is the common radius of the two contacted particles. The interparticle friction angle governing the Coulomb friction criterion is set to be $\phi = 0.5$ rad. The density of the particles is set to $\rho_{\text{cl}} = 2650$ kg/m³. The DEM implementation of the clumps is similar to Šmilauer *et al.* (2010).

Two macroscopic quantities pivotal to the multiscale computation, the tangent modulus and the Cauchy stress tensor, are homogenised from the RVE packing at each Gauss point. By adopting a uniform strain assumption (Wren & Borja, 1997; Krut & Rothenburg, 1998; Luding, 2004), the tangent modulus used for iterative solution of equation (2) is estimated as

$$D_{ijkl} = \frac{1}{V} \sum_{c \in N_c} \left(k_n n_i^c d_j^c n_k^c d_l^c + k_t t_i^c d_j^c t_k^c d_l^c \right) \quad (4)$$

where V is the total volume of the assembly, N_c is the total contact number in the assembly, \mathbf{n}^c is the outward contact normal, \mathbf{d}^c is the branch vector connecting the centres of the two contacted clumps (see Fig. 1). \mathbf{t}^c is the unit vector along the tangential direction of a contact. The Cauchy stress tensor is evaluated from the Love's formula:

$$\sigma_{ij} = \frac{1}{V} \sum_{c \in N_c} d_i^c f_j^c \quad (5)$$

where \mathbf{f}^c is the interparticle contact force. From σ_{ij} , the mean effective stress p and the deviatoric stress q can be calculated (in two dimensions): $p = \sigma_{ii}/2$, $q = \sqrt{s_{ij}s_{ji}}/2$ ($s_{ij} = \sigma_{ij} - p\delta_{ij}$, δ_{ij} denoting the Kronecker delta). The local strain is measured from the displacement gradient (obtained from the FEM solution), namely $\boldsymbol{\varepsilon}_{ij} = -(u_{i,j} + u_{j,i})/2$. Accordingly, the volumetric and deviatoric strains can be defined: $\varepsilon_v = \boldsymbol{\varepsilon}_{ii}$, $\boldsymbol{\varepsilon}_q = \sqrt{2\boldsymbol{e}_{ij}\boldsymbol{e}_{ji}}$, where $\boldsymbol{e}_{ij} = \boldsymbol{\varepsilon}_{ij} - \varepsilon_v\delta_{ij}/2$. The rigid body rotation (note that the rigid body rotation is specifically referred to the overall rotation of the RVE

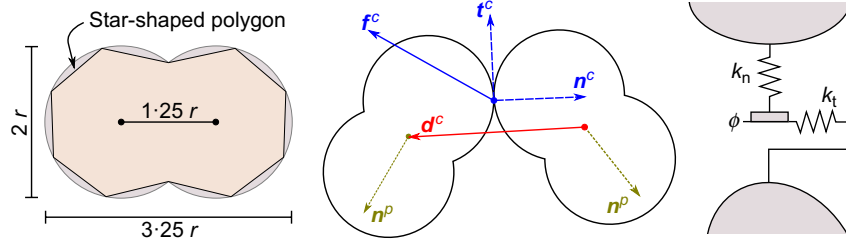


Fig. 1. Clump geometry and interparticle contact law

packing here) $\omega_{ij} = (u_{j,i} - u_{i,j})/2$ is also considered for the RVE boundary condition to accommodate large deformations in strain localisation.

Quantification of fabric anisotropy

According to Casagrande & Carillo (1944), granular soils commonly possess two forms of anisotropy, namely, inherent anisotropy and induced anisotropy (see also Arthur & Menzies, 1972; Arthur *et al.*, 1977; Wong & Arthur, 1985). Inherent anisotropy is formed due to preferentially oriented particles, voids and contact normals during geological deposition processes such as tectonic compaction and hydraulic/pneumatic transport or laboratory sample preparation through air/water pluviation. Induced anisotropy is caused by the applied loading, which may alter the pre-existing inherent anisotropy and induce rearrangements of the soil fabric. Both types of anisotropy affect the overall behaviour of sand significantly (Oda, 1972a, 1972b; Abelev & Lade, 2003; Lade & Abelev, 2003; Hasan & Alshibli, 2010; Guo & Zhao, 2013b; Zhao & Guo, 2013). This paper adopts the fabric tensor to quantify both sources of soil anisotropy. Prior to loading, the fabric tensor represents the state of inherent (or more accurately, initial) anisotropy in sand, whereas upon loading, it reflects the superposition of inherent anisotropy and induced anisotropy. In particular, two different definitions of fabric tensor are compared. One follows the widely used definition proposed by Satake (1982) and Oda (1982) based on the contact normal distribution (ϕ_{ij}^c), and the other is defined based on the particle orientation (ϕ_{ij}^p)

$$\phi_{ij}^* = \int_{\Theta} E(\Theta) n_i^* n_j^* d\Theta = \frac{1}{N_*} \sum_{N_*} n_i^* n_j^* \quad (* = c, p) \quad (6)$$

where the super/subscript * denotes either 'c' or 'p' for the two tensors (throughout this paper). n^p is a unit vector pointing along the longest axis of the clump (see Fig. 1). N_p is the total number of clumped particles in the assembly. The distribution function $E(\Theta)$ can be approximated by a second-order truncation of its Fourier expansion

$$E(\Theta) = \frac{1}{2\pi} \left(1 + F_{ij}^* n_i^* n_j^* \right) \quad (* = c, p) \quad (7)$$

where the deviatoric tensors F_{ij}^c and F_{ij}^p quantifying the fabric anisotropy can be calculated

$$F_{ij}^* = 4 \left(\phi_{ij}^* - \frac{1}{2} \delta_{ij} \right) \quad (* = c, p) \quad (8)$$

A scalar F_c or F_p can be used to measure the anisotropic intensity

$$F_* = \sqrt{\frac{1}{2} F_{ij}^* F_{ij}^*} \quad (* = c, p) \quad (9)$$

Preparation of RVEs

A DEM assembly containing 400 particles proves to be sufficient for the RVE (see also Guo & Zhao, 2013a, 2014; Nguyen *et al.*, 2013, 2014) and is used in the study. Each RVE contains clumps of equivalent radii ranging from 3 mm to 7 mm with particle size distribution (PSD) according to Fig. 2(a). All particles (indeed rods) are assumed to have a thickness of 100 μ m, that is about

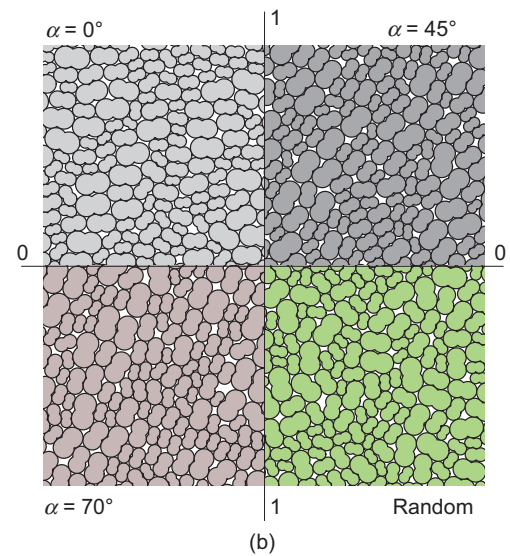
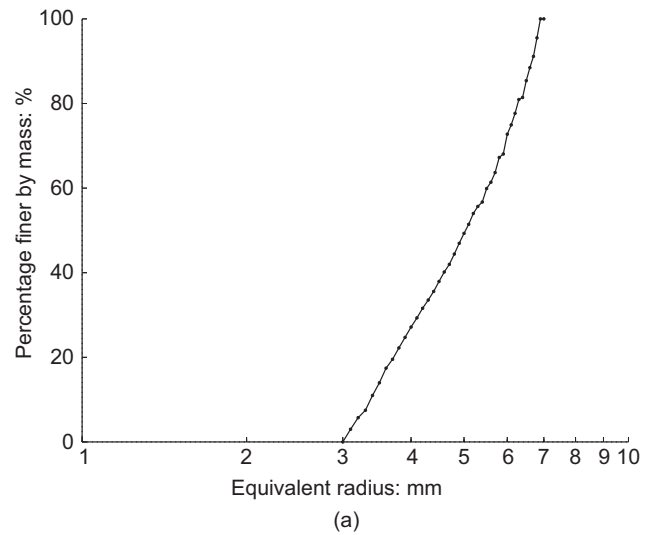


Fig. 2. (a) PSD of the RVE assembly; (b) snapshots of four isotropically consolidated RVEs (partial) with different bedding plane angles

ten times the mean particle diameter. With the assumed thickness, the stress quantities in the current two-dimensional (2D) simulations are rendered in pressure units (i.e. force over area). To prepare RVEs with different inherent anisotropies, an assembly is generated with all particles orientated in the same direction with no overlap. Their orientation with regard to the horizontal plane (the $0-0$ axis) is denoted by an angle α , which is hereafter referred to as the bedding plane angle. A two-stage isotropic consolidation is then applied. First, the rotational degrees of freedom (RDOFs) of all particles are prohibited until a first-stage consolidation pressure $p = 50$ kPa is reached. A second stage of consolidation is then continued by relaxing the RDOFs for all particles until the sample reaches a final designated pressure $p_0 = 100$ kPa. During both stages, the interparticle friction angle is set small and is adjusted case by case to obtain different dense packings with a close initial void ratio of around $e_0 = 0.13$. A total of five RVE packings, with $\alpha = 0^\circ, 22.5^\circ, 45^\circ, 70^\circ$ and a randomly orientated packing, respectively, are prepared as shown in Fig. 2(b). During the multiscale simulations, periodic boundary conditions are imposed on each of the local RVE assemblies, which renders the Hill–Mandel-type condition satisfied a priori (Miehe & Dettmar, 2004; Miehe *et al.*, 2010). Note that in a pure DEM study, proper observation windows (see e.g. Meejun *et al.*, 2008; Fu & Dafalias, 2011a) need to be defined for macroscopic interpretations. They are not required in the current multi-scale approach since the mesoscale RVE packings serve a better role in this regard.

Figure 3 presents the homogenised responses of the five RVEs under drained biaxial compression (note that the two vertical sides of the unit cell are kept with constant confining pressure of 100 kPa, and the top/bottom is fixed against the vertical direction while allowing horizontal movement when compression is applied from the top), mimicking the subsequent biaxial shear on the full sample under smooth platen. The RVE responses are consistent with laboratory observations on sand. The peak stress of the RVE decreases steadily with the increase of α . The $\alpha = 0^\circ$ RVE packing shows the most dilative response accompanied with a drastic post-peak softening behaviour, whereas the dilation and the softening for the $\alpha = 70^\circ$ RVE are relatively mild. The random packing gives rise to an intermediate strength and dilation behaviour among all the RVEs. Note that the observed responses in Fig. 3 are similar to those obtained by Seyed Hosseininia (2012a, 2012b) using elongated polygonal particles.

Model set-up for multiscale simulation of biaxial shear on sand

The influence of anisotropy on strain localisation is investigated through multiscale modelling of biaxial compression tests on sand. Two boundary conditions are compared, using either smooth or rough loading platens on the sand samples. A sand specimen with dimensions 50 mm by 100 mm is discretised into 8×16 eight-node quadrilateral elements, as shown in Fig. 4. A reduced integration scheme using 2×2 Gauss points for each element is adopted, which provides good accuracy compared to the full integration using 3×3 Gauss points to be shown in Fig. 6(a). The specimen is initially uniform by assigning identical RVEs to all Gauss points. It is first isotropically consolidated to a target initial mean effective pressure $p_0 = 100$ kPa, and is then compressed along the vertical direction with a constant horizontal confining pressure $\sigma_{00} = 100$ kPa until it fails.

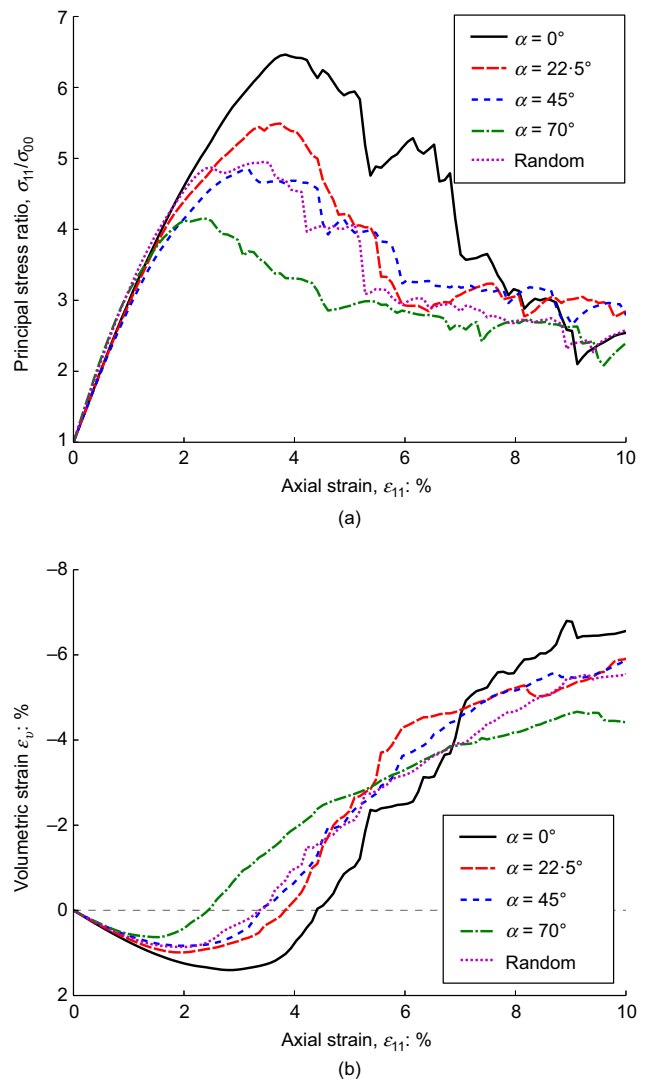


Fig. 3. Responses of different RVEs under drained loading condition: (a) stress–strain relations; (b) dilatancy curves

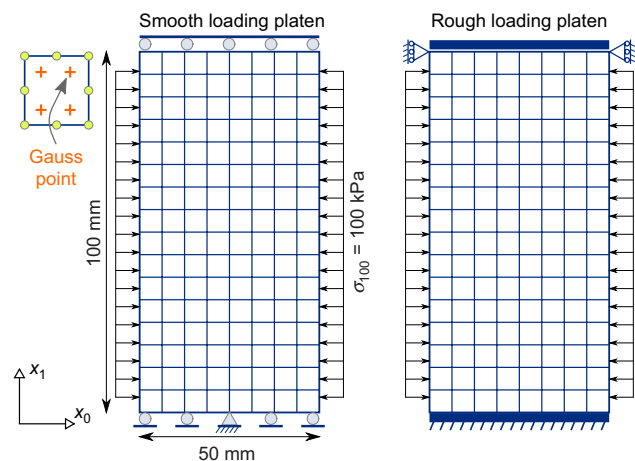


Fig. 4. FEM mesh containing 8×16 eight-node quadrilateral elements and boundary conditions for the biaxial compression tests

RESULTS AND DISCUSSION

Global stress response

Figure 5 provides the resultant global axial stresses (compression is positive) plotted against axial strain for different specimens under different loading conditions, in

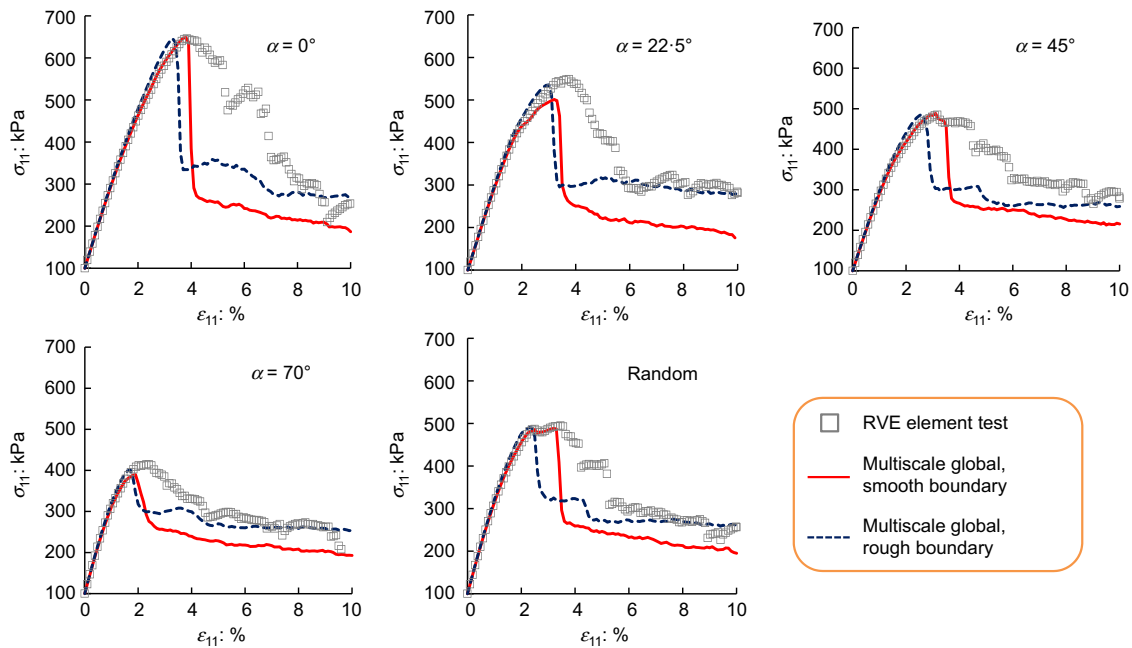


Fig. 5. Global axial stress from the multiscale simulations with different boundary conditions in comparison with the RVE element responses

comparison with pure RVE element test results. Fig. 6 further compares the global resultant stress of the five specimens in both loading cases. Owing to the use of the rough loading platen, shear stresses are also resulted in the rough platen case (Fig. 6(c)). In both cases, the general trend of the peak axial stress of the five specimens is consistent with that of the RVEs; that is, the peak axial stress decreases with the increase of α . However, the post-peak stress reduction in the multiscale simulation is more dramatic than that in RVE element test, due to the formation of a shear band in the multiscale BVP. Similarly to their respective RVE, the five specimens reach a comparable residual stress (around 200 kPa in the smooth case and 300 kPa for the rough case). The pre-peak responses of the multiscale simulation for both boundary cases coincide well with their corresponding RVE responses for all the samples, especially during the early elastic stage. For the cases of $\alpha=0^\circ$, 45° and the randomly orientated specimens, the multiscale global peak axial stress is almost identical to their respective RVE peak stress, suggesting a relatively uniform pre-peak deformation in these specimens. The other two samples ($\alpha=22.5^\circ$ and 75°) exhibit a smaller multiscale global peak axial stress that occurs earlier than their RVE peak stress under both loading conditions, which indicates that considerable strain localisation may have developed prior to the peak in these samples. Fig. 5 also shows that the peak stress is attained slightly earlier in the rough loading condition than in the corresponding smooth case.

The post-peak responses display a marked difference between the rough and smooth loading cases. The axial stress in the smooth case (Fig. 6(a)) first drops dramatically after the peak and then becomes steady, while in the rough platen condition (Fig. 6(b)), it first shows a dramatic drop after peak before entering a quasi-steady state, and then increases to a mild second peak before dropping again to a final steady value. These subtle post-peak changes in Fig. 6(b) are intimately correlated with the development of the resultant shear stress as shown in Fig. 6(c). During the early shearing stage, the resultant shear stress in most specimens (except the $\alpha=70^\circ$ sample) remains vanishingly small because the deformation in each specimen is still symmetric. The first dramatic drop in Fig. 6(b) indeed corresponds to a rapid increase of the resultant shear stress,

while the second mild peak of the normal stress coincides with the maximum shear stress. Towards the final steady state, the resultant shear stress tends to vanish gradually. The magnitude of the resultant shear stress is generally an order smaller than that of the axial stress.

Figure 6(a) also shows for the smooth case of the $\alpha=0^\circ$ sample, the predictions based on a reduced integration scheme with 2×2 Gauss points (solid line) are almost identical with those obtained from a full integration scheme with 3×3 Gauss points (open circles). This indicates that the high-order eight-node element with reduced integration is accurate enough while improving computational efficiency.

Strain localisation and shear band patterns

The multiscale simulations show that a single shear band is exclusively observed under the smooth loading condition, whereas a cross-shaped double band pattern is found for the rough platen case. Fig. 7 shows contours of the accumulated deviatoric strain ε_q and void ratio e at the peak stress state, and the final state for three specimens in both loading cases. Under smooth loading conditions (Figs 7(a) and 7(b)), the deformation of the $\alpha=45^\circ$ sample at the peak stress state remains relatively homogeneous (small range in ε_q and e), while the $\alpha=22.5^\circ$ specimen already shows a greater variation of ε_q and e at the peak, suggesting that localisation has developed at the peak, which results in a smaller global peak stress than the RVE element test (Fig. 5). An intensely localised shear band coinciding with the greatest void ratio is observed in both samples at the final stage with accumulated ε_q reaching 172~198%. The minimum ε_q at the final state in both samples is also smaller than that in the peak stress state, indicating unloading in regions outside the shear band. Interestingly, a shear band inclining closely to the bedding plane direction (termed as a type-b band according to Tatsuoka *et al.* (1990)) is observed in the $\alpha=22.5^\circ$ sample, while the one in the $\alpha=45^\circ$ sample is more to the perpendicular direction of the bedding plane (termed by Tatsuoka *et al.* (1990) as a type-a band). Both types of shear band have been reported by Tatsuoka *et al.* (1986, 1990) in their plane strain tests with lubricated loading platen. It was argued that the type-a shear band is typically governed by the

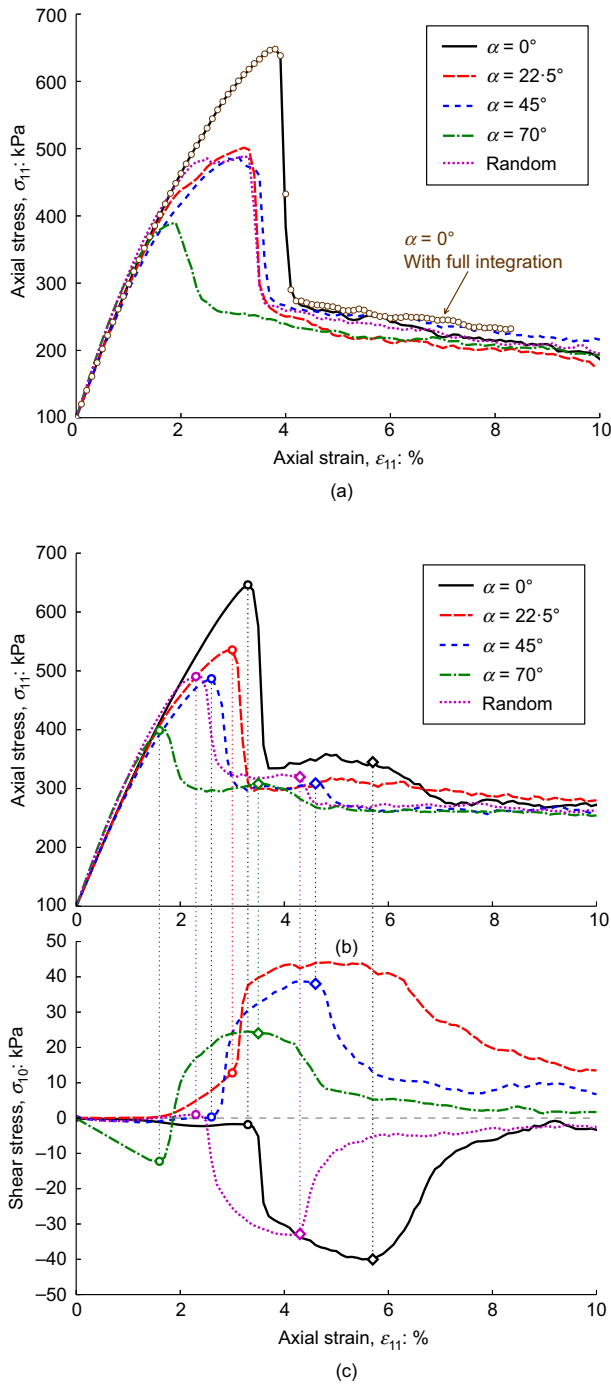


Fig. 6. (a) Resultant normal stress with smooth loading platen; resultant (b) normal and (c) shear stresses with rough loading platen

Coulomb's failure condition, whereas the type-b band is controlled by the zero-extension failure mechanism (Tatsuoka *et al.*, 1990; Gao & Zhao, 2013).

Under rough loading conditions, a cross-shaped shear band pattern is appreciable in the $\alpha = 45^\circ$ sample at the peak axial stress state, although the intensity of shear strain remains low. Shear stress with symmetric distribution is resulted along the top end of the sample by the loading platen constraint (Fig. 7(c)) and the net shear stress is zero (Fig. 6(c)). The type-b shear band develops dominantly after the peak axial stress, while the type-a band stays nearly stagnant until the resultant shear stress reaches its peak. After the peak shear stress state, the type-a shear band restarts to develop with the type-b band. At the final stage ($\epsilon_{11} = 10\%$), the shear stress approaches zero and an almost

symmetric (in shape) crossed double shear band pattern is observed, with the first developed type-b band showing more intense shear strain concentration than the type-a band. Regarding the $\alpha = 70^\circ$ sample, this exhibits an initial non-coaxial material response from the beginning, leading to a steady increase in the resultant shear stress and an asymmetric shear deformation (Fig. 7(d)). The type-b shear band is dominant over the type-a band until the peak shear stress state is reached ($\epsilon_{11} = 3.6\%$). The subsequent development of the shear bands is similar to that of the $\alpha = 45^\circ$ case, except that the final cross shear band pattern appears to be slightly asymmetric.

Fabric anisotropy and particle rotation

In addition to the accumulated shear strain and the void ratio, it is also interesting to examine the distribution of fabric anisotropy and the average particle rotation. Fig. 8 presents the results at the final stage for two samples under smooth loading conditions and two samples in the rough case, wherein the average particle rotation within a DEM packing is defined by

$$\bar{\theta} = \frac{1}{N_p} \sum_{p \in N_p} \theta^p \quad (10)$$

where θ^p is the accumulated rotation of an individual particle (anti-clockwise rotation is treated as positive).

For the smooth case, it is evident from Figs 8(a) and 8(b) that the contours of both F_p and $\bar{\theta}$ present rather similar patterns to those of ϵ_q and e in Figs 7(a) and 7(b). The localised $\bar{\theta}$ suggests substantial particle rotations inside the shear band. This is consistent with both laboratory experiments (Hall *et al.*, 2010) and pure DEM simulations (Bardet & Proubet, 1991). Notably, $\bar{\theta}$ is anti-clockwise in the case of $\alpha = 22.5^\circ$ and is clockwise in the random case. This is not surprising since the shear band develops from the upper-right to the lower-left side in the $\alpha = 22.5^\circ$ case, whereas it inclines from the upper-left corner to the lower-right corner in the random specimen. Despite these similar localised patterns, the two samples exhibit different behaviour in F_p . The $\alpha = 22.5^\circ$ specimen possesses a relatively large initial anisotropic intensity compared to the random case. F_p inside the localised band decreases with shearing and reaches a minimum as compared to the outside regions. In contrast, the random sample has a marginally small initial fabric anisotropy ($F_p \approx 0$), and its F_p gradually increases inside the shear band upon shearing and reaches a maximum at the final stage. Fig. 8(c) presents the contours of the deviatoric stress q and the contact normal based fabric anisotropy F_c , which indicate both are apparently unsuitable to identify the shear band (see also Guo & Zhao, 2014).

Under rough boundary conditions, the contours of F_p and $\bar{\theta}$ for the two specimens (Figs 8(d) and 8(e)) also depict similar localisation patterns as shown by ϵ_q and e . The $\alpha = 70^\circ$ specimen, with a higher initial fabric anisotropy, shows a continuously decreasing F_p inside the double shear bands upon shearing, whereas the F_p in the random specimen (with a nearly zero initial anisotropy) increases gradually under shear and reaches a maximum within the localised bands. The contours of F_p show a similar pattern as observed before that one shear band dominates the other. The two samples share similar contours of $\bar{\theta}$. Anti-clockwise rotation (positive $\bar{\theta}$) is found for particles inside the type-b band, and clockwise rotation (negative $\bar{\theta}$) is observed within the type-a shear band. At the intersection of the two bands, the particles possess almost zero average accumulated rotation. Since the two shear bands have developed asynchronously, the particles at this centre location are expected to rotate towards

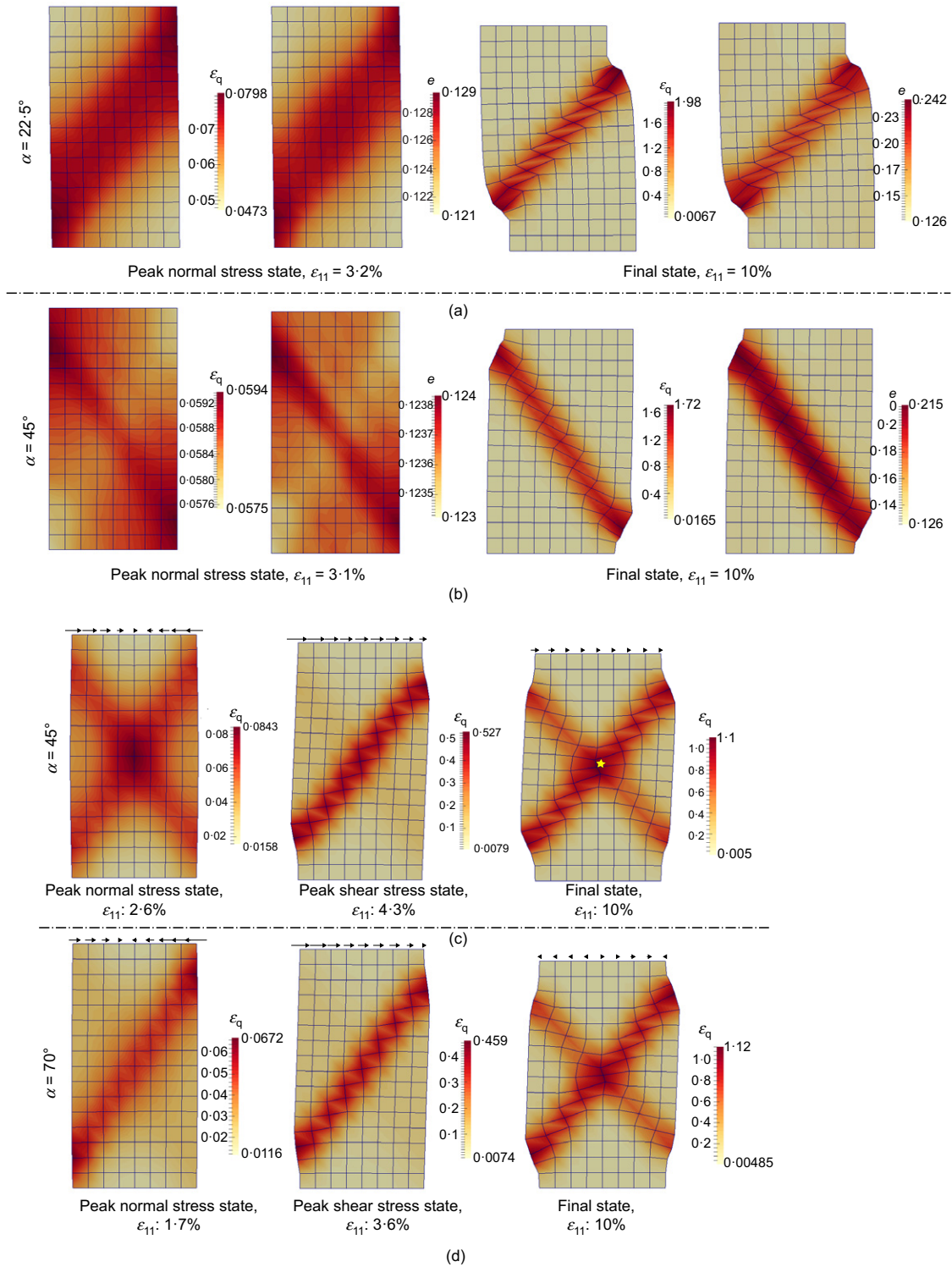


Fig. 7. Contours of the accumulated deviatoric strain and the void ratio for specimens under (a), (b) smooth and (c), (d) rough loading conditions at different shearing levels. Note the difference in the shading ranges

one direction first, and then rotate inversely when the second shear band becomes distinct.

Non-coaxiality

All simulations in this paper have been based on initially uniform specimens with symmetric boundary conditions. In a conventional FEM analysis, such samples are expected to undergo homogeneous deformation without observing any localisation. Most past studies have practically introduced

either imperfections or random fields for elements/material parameters as triggers to simulate shear banding (Andrade & Borja, 2006; Andrade *et al.*, 2008; Tejchman & Górski, 2010). Despite being partially justified by the random nature of geomaterials, these treatments may appear to be subjective and potentially complicate the analysis of underlying mechanisms with the random factors introduced. Indeed, the non-coaxial response of a granular material induced by the presence of anisotropy can play a role of symmetry breaker to trigger strain localisation, which has been

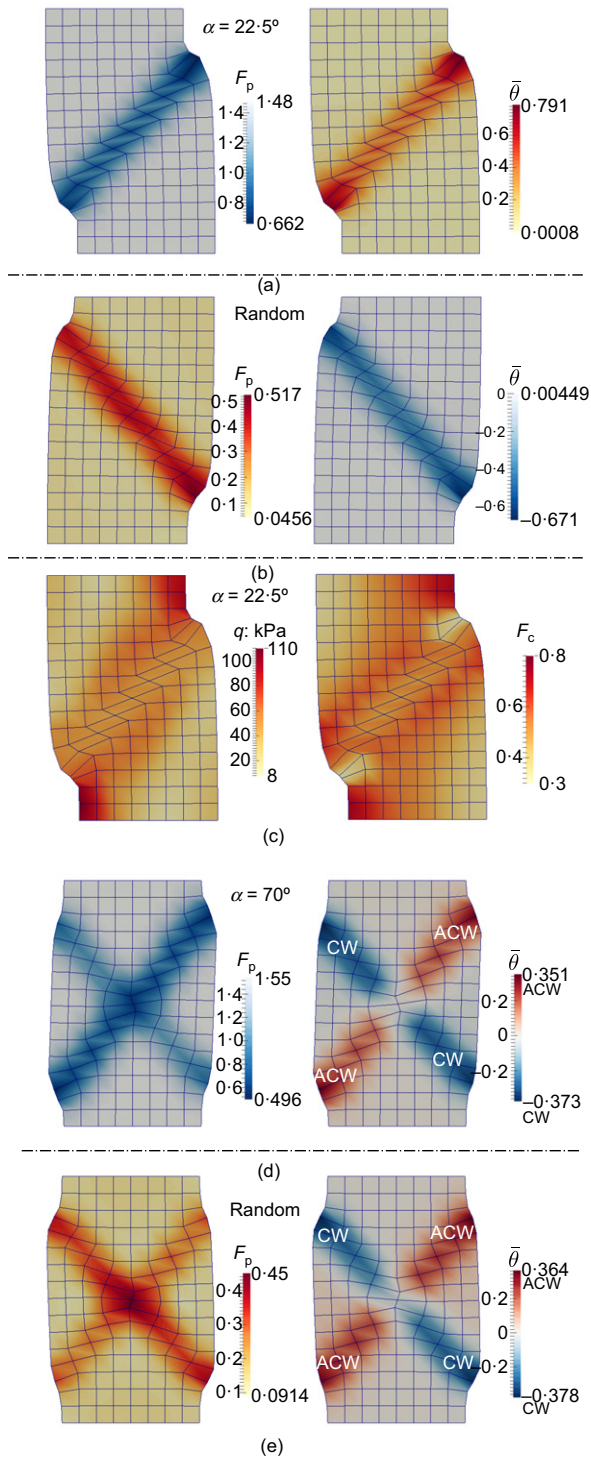


Fig. 8. Contours of F_p , $\bar{\theta}$, q and F_c for specimens under (a)–(c) smooth and (d), (e) rough loading conditions at $\varepsilon_{11} = 10\%$. For colour interpretation of this figure, readers are referred to the web version of this paper (ACW: anti-clock wise; CW: clock wise)

demonstrated by Gao & Zhao (2013) and Guo & Zhao (2014). By virtue of its embedded DEM engine for each Gauss point, the multiscale modelling can naturally reproduce the non-coaxial response of a granular soil, and helps to capture strain localisation without resorting to introducing any artificial imperfection or randomness. The smooth platen loading case is taken here as an example.

Figure 9 presents the material responses of three RVEs ($\alpha = 22.5^\circ$, 45° and 70°) based on their *element test* (note that the element tests are performed on the unit cell).

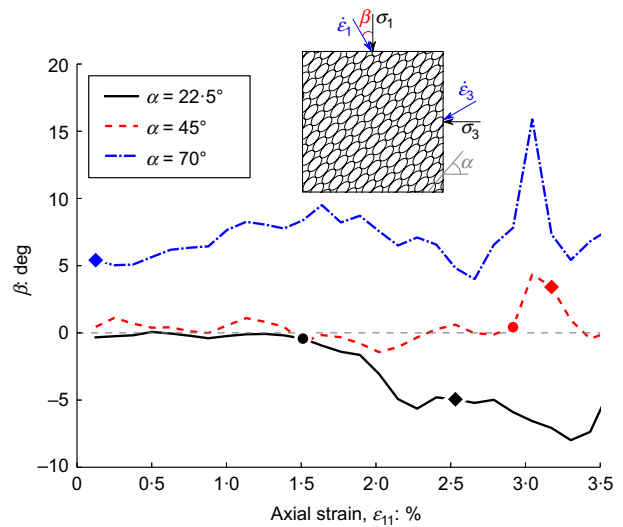


Fig. 9. Non-coaxial responses of the RVEs. The inset illustrates the definition of the non-coaxiality angle, β

Notwithstanding the fluctuated response curves due to a limited number of particles used, the non-coaxial behaviour is evident for each RVE. The non-coaxiality angle β (see the inset of Fig. 9) is defined as the angle between the major principal stress direction and the major principal strain increment direction. Notably, both $\alpha = 22.5^\circ$ and $\alpha = 45^\circ$ RVEs depict a roughly coaxial response ($\beta \approx 0^\circ$) at the early shearing stage up to an axial strain of about 1.55% and 3%, respectively. After $\varepsilon_{11} = 1.55\%$, the $\alpha = 22.5^\circ$ RVE gradually develops a negative β , which triggers a type-b shear band as observed in Fig. 7(a), whereas the $\alpha = 45^\circ$ RVE develops a positive β after $\varepsilon_{11} = 3\%$, leading to the formation of the type-a shear band shown in Fig. 7(b). The $\alpha = 70^\circ$ RVE demonstrates a positive non-coaxiality from the very beginning of shearing, which leads to a type-a shear band. The material non-coaxiality observed from the element tests is indeed consistent with the global responses in the BVPs. Shown in Fig. 10 are the accumulated displacement fields for the three specimens at different shearing levels. For example, the displacement field in the $\alpha = 22.5^\circ$ specimen remains symmetric at $\varepsilon_{11} = 1.5\%$ as the material response is coaxial (Fig. 9). When the axial strain reaches 2.5%, an appreciable leftwards-inclined displacement field is found, which triggers a type-b shear band shortly after.

Clearly, the non-coaxiality observed in the RVEs is not predetermined by the bedding plane orientation, but is a consequence of the interplay among several key factors including the particle orientation, the contact normal distribution, the bulk density and the particle interlocking. Indeed, the two fabric tensors ϕ_{ij}^p and ϕ_{ij}^c for soil are usually orthogonal to each other. In the bedding plane direction, there are less contact normals (n^c) but longer branch vectors (d^c), while in the perpendicular direction of the bedding plane there are more n^c but shorter d^c . The number of contact normals and the length of branch vectors can be identified as two major competing factors in determining non-coaxiality, since they directly influence the principal directions of the tangent modulus D_{ijkl} in equation (4), which predominantly governs the material non-coaxial response.

Local analyses

The hierarchical multiscale approach enables a direct correlation of the macroscopic observations with their underlying microstructural mechanisms through local

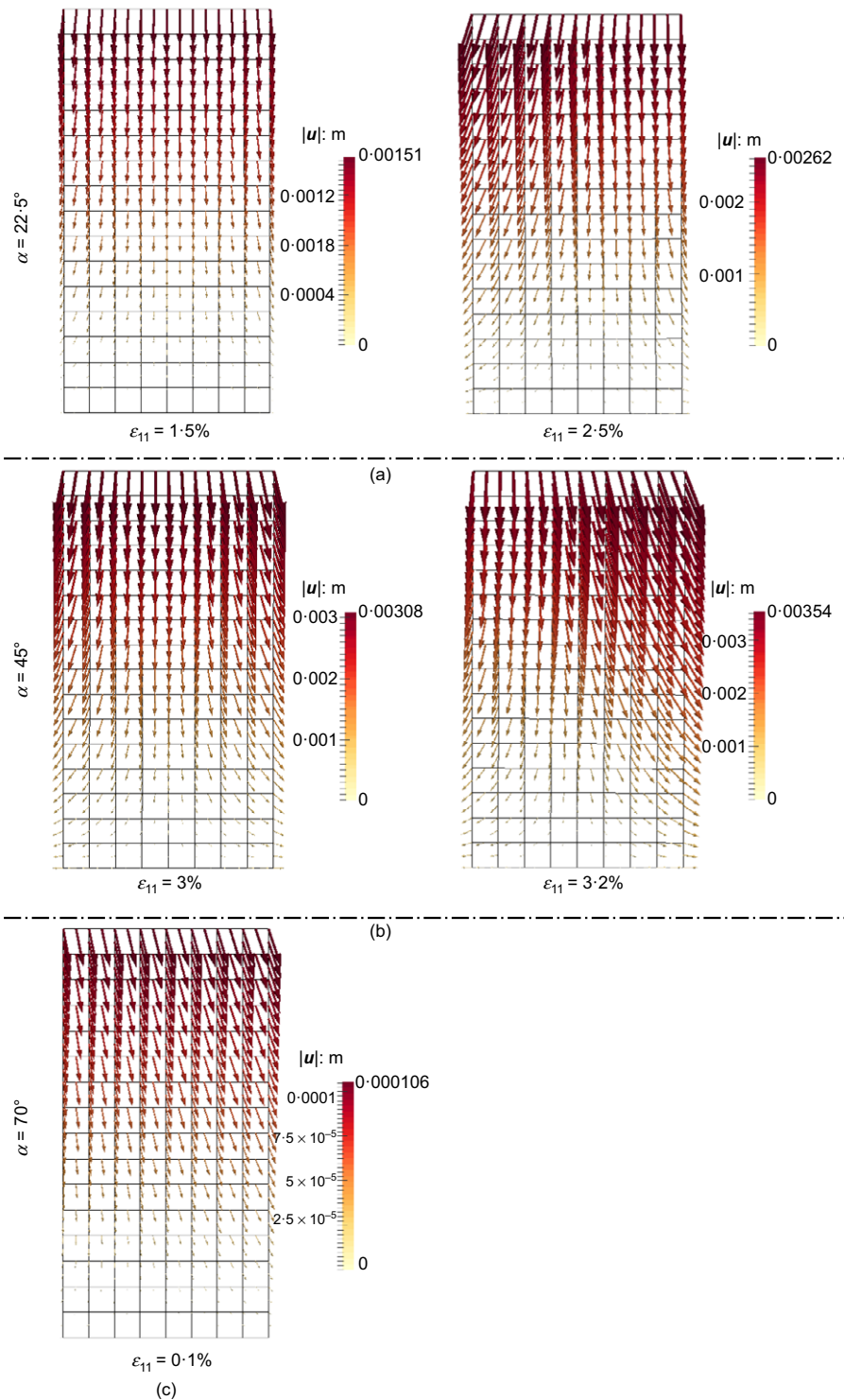


Fig. 10. Accumulated displacement field for: (a) $\alpha = 22.5^\circ$; (b) $\alpha = 45^\circ$; (c) $\alpha = 70^\circ$ specimens at different shearing levels

analyses. Take the $\alpha = 0^\circ$ sample in the smooth boundary case as an example. Two typical local points, as shown in Fig. 11(e), are selected for the analysis. Gauss point A is located far away from the localisation zone, while the Gauss point B is inside the shear band. Figs 11(a)–11(c) show the material responses of point A extracted from the corresponding RVE. Clearly, point A undergoes a small deformation, reaching a maximum shear strain $\epsilon_q = 6.4\%$ followed by unloading. The loading path in Fig. 11(b) indicates the stress of point A almost returns to its initial isotropic state after the unloading. The overall volumetric change is also small ($\epsilon_v = -0.4\%$). During the process, F_p at point A stays

almost unchanged, while F_c first experiences a significant increase during the loading stage and then decreases during unloading. The force chain network of the embedded RVE packing of point A at the final stage, shown in Fig. 11(d), is almost isotropic. In contrast to point A, point B experiences excessively large deformation as shown in Figs 11(f)–11(i). Its deviatoric strain monotonically increases to around 200%, reaching the critical state (Roscoe *et al.*, 1958; Schofield & Wroth, 1968) when the stress, the volume and both fabric anisotropies all become constant. The material responses at point B match reasonably well with the results of a comparison pure DEM case under monotonic drained

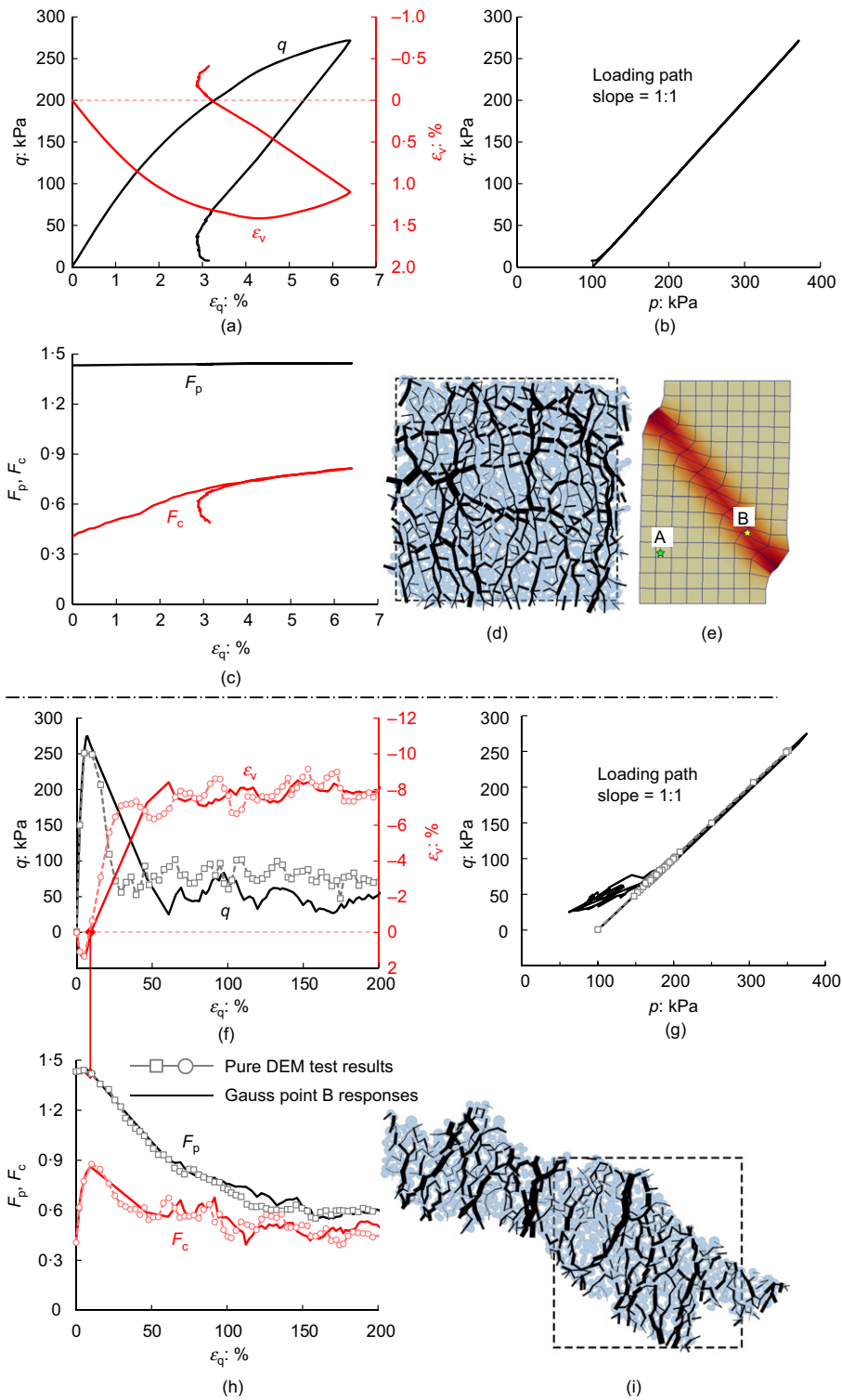


Fig. 11. Local Gauss points responses in the $\alpha=0^\circ$ specimen: (a)–(c) Gauss point A responses; (d) RVE force chain of Gauss point A after shear; (e) locations of the two Gauss points in the deformed mesh; (f)–(h) Gauss point B responses; (i) RVE force chain of Gauss point B after shear. Note the force chain width is proportional to the contact normal force and the width in (d) is scaled two times wider than that in (i) for better visualisation

shear shown in Figs 11(f)–11(h) (open symbols). When both F_p and F_c evolve with shear strain, the zero- ϵ_v point (from overall contraction to dilation) at around $\epsilon_q=9.5\%$ can be regarded as a watershed point in observing their changes. F_c increases steadily upon shearing, attains a peak of more than twice its initial value at the watershed point, and then drops gradually before reaching a steady value. Prior to the watershed strain level, F_p only shows marginally small increase, and then decreases to a steady value of around 40% of its peak.

The above observations suggest that F_p is generally harder to mobilise than F_c . In order for F_p to change, in addition to shearing, considerable dilation is needed to allow the relaxation of interlocking and reorientation of particles, which is in contrast to the immediate change of F_c upon shearing. The evolutions of the two sources of fabric anisotropy are hence not synchronous. This probably helps to explain the previous observations on the $\alpha=22.5^\circ$ and the $\alpha=45^\circ$ samples in Fig. 9 that an initially coaxial packing may later develop substantial non-coaxiality. Notably, it also

takes a significant shearing process for F_p to reach its critical state (e.g. $\varepsilon_q > 150\%$ for point B). This large deformation level is normally hard to attain in a uniform sample in routine laboratory element tests, which partially explains why Oda (1972b) and Wong & Arthur (1985) observed in their tests the survival of inherent anisotropy and limited particle orientation change (Wong & Arthur (1985) only sheared their soil samples to 6% of axial strain). Meanwhile, the above analysis suggests that, although the stress and volumetric changes can reach a steady state at a relatively early stage (e.g. $\varepsilon_q \approx 60\%$ in Fig. 12(f)), the critical state for fabric anisotropy (Li & Dafalias, 2012; Zhao & Guo, 2013; Gao *et al.*, 2014) can only be attained within the shear band wherein much larger shear deformation occurs (e.g. $\varepsilon_q > 100\%$) (Mooney *et al.*, 1998; Fu & Dafalias, 2011a). Indeed, as shown in Fig. 11(i), the RVE packing at point B experiences severe distortion (c.f. Fig. 11(d) for point A) at the final stage accompanied by a significant clockwise rigid body rotation ω_{ij} . The force chain network in Fig. 11(i) also contains several penetrating strong force chains in the vertical compression direction.

To further elucidate the natures of the two fabric tensors ϕ_{ij}^p and ϕ_{ij}^c , in Fig. 12 their evolution is presented in terms of rose diagrams extracted from a RVE inside the shear band formed in the $\alpha = 0^\circ$ specimen and the random specimen under smooth loading conditions. The RVE for the $\alpha = 0^\circ$ case (Fig. 12(a)) possesses large initial anisotropies for both measures. The major principal direction of the initial ϕ_{ij}^p aligns in the horizontal axis, which is almost perpendicular to the major principal direction of the initial ϕ_{ij}^c . After shear, the major direction of ϕ_{ij}^p rotates noticeably with a decreased anisotropic intensity, but the rotation of ϕ_{ij}^c and its change of

intensity is relatively small. For the randomly orientated sample shown in Fig. 12(b), the RVE possesses nearly isotropic fabric tensors at the initial state (both ϕ_{ij}^p and ϕ_{ij}^c depict minor anisotropies due to the limited number of particles used). After shear, the intensity of both anisotropy measures increases. At the final stage, the major principal directions of the two fabric tensors are roughly perpendicular to each other. A further scrutiny of the fabric tensors at the critical state from both specimens suggests that, although different in initial states, their critical state fabric anisotropies are close in terms of both principal direction (the small deviation in the principal orientations of ϕ_{ij}^p is attributable to the different rigid body rotation ω_{ij} of the two RVE packings) and anisotropic intensity (the length of the major principal axis observed from Fig. 12 is about 0.25 for ϕ_{ij}^p and 0.23 for ϕ_{ij}^c , noting that different radial length scales have been used for ϕ_{ij}^c in the two cases).

A particularly interesting observation for the rough boundary case is the material response at the intersection of two crossed shear bands. Fig. 13 shows the results of such a point for the $\alpha = 45^\circ$ specimen whose position is marked in Fig. 7(c). The material responses at the Gauss point in Figs 13(a)–13(c) match fairly well with the results of a monotonically drained pure DEM test as a comparison case. The point appears to reach the critical state after the deviatoric strain reaches 120%. Fig. 13(d) presents the force chain network of the RVE packing at the peak shear stress ($\varepsilon_{11} = 4.3\%$, corresponding to the onset state of the second shear band), which depicts a noticeable anti-clockwise rigid body rotation ω_{ij} that is consistent with the first shear band (type-b) of the specimen. At the final state, the RVE packing is severely deformed, but the rigid body rotation becomes

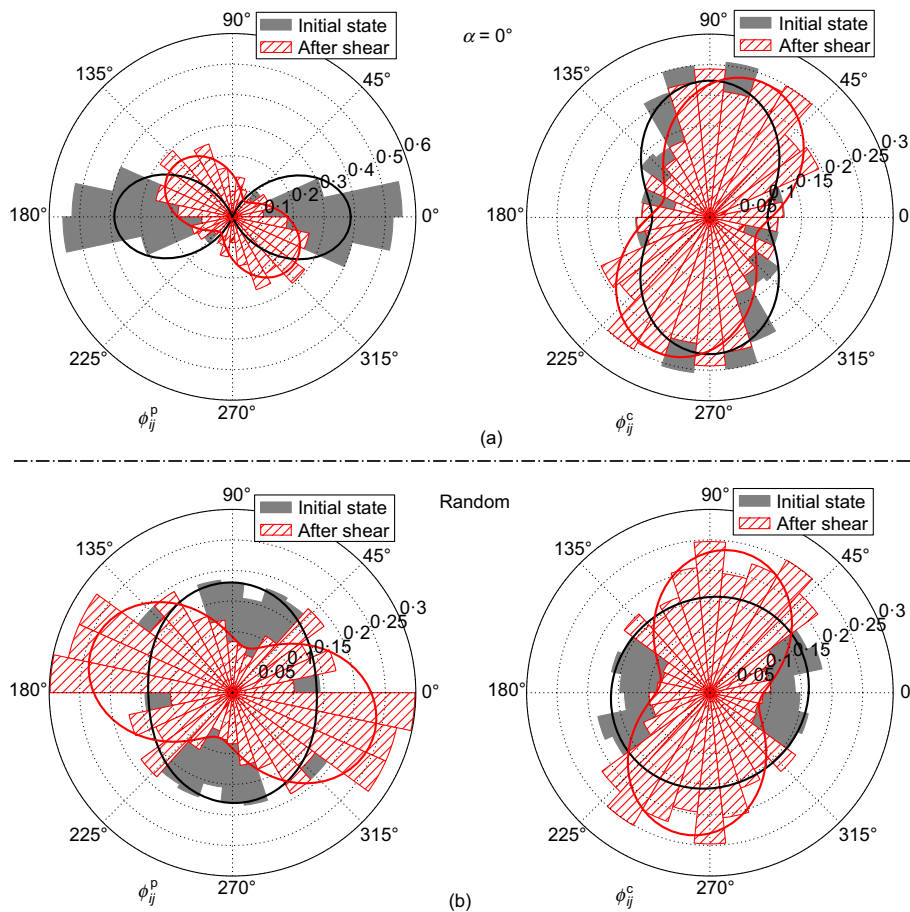


Fig. 12. Evolution of the two fabric tensors ϕ_{ij}^p and ϕ_{ij}^c for RVEs inside shear band in (a) the $\alpha = 0^\circ$ and (b) the randomly orientated specimens. Note the difference in the radial length scales

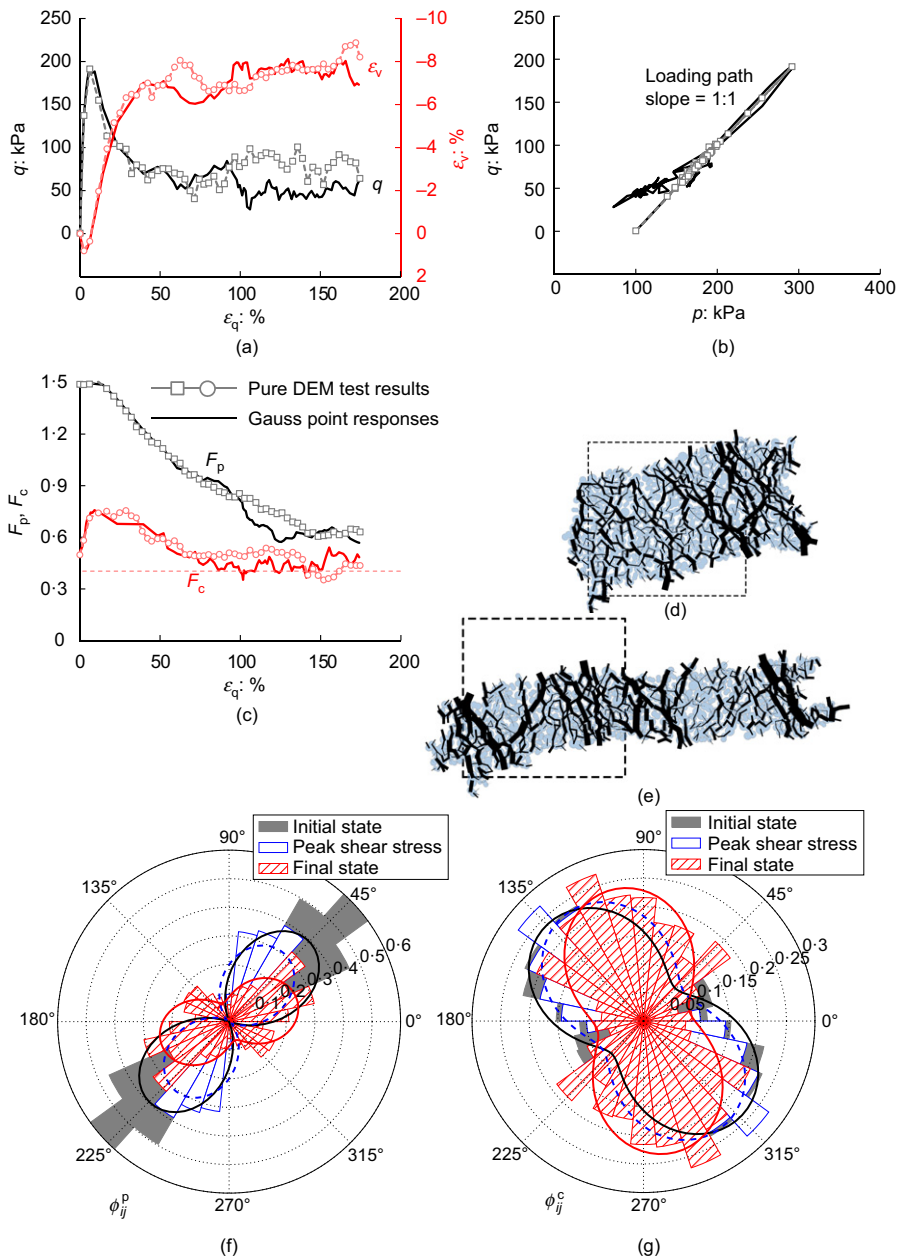


Fig. 13. Local Gauss point (position marked in Fig. 7(c)) responses in the $\alpha = 45^\circ$ specimen: (a)–(c) evolution curves; (d) and (e) RVE force chains; (f) and (g) fabric tensors ϕ_{ij}^p and ϕ_{ij}^c at different shearing levels respectively

negligible again due to the balance of the second shear band (Fig. 13(e)). The observation is consistent with the observed zero $\bar{\theta}$ at this point in Fig. 8. Meanwhile, strong force chains are observed for the RVE in Figs 13(d) and 13(e), with the major direction slightly tilted from the vertical axis. The evolutions of the two fabric tensors are also presented in Figs 13(f) and 13(g). Interestingly, ϕ_{ij}^p first flips anti-clockwise slightly until the peak shear stress state due to the rigid body rotation of the RVE. It then spins clockwise significantly to attain the critical state. The anisotropy intensity of ϕ_{ij}^p decreases steadily to a critical state value (see also Fig. 13(c)), while ϕ_{ij}^c rotates continuously clockwise to the critical state with a roughly constant anisotropic intensity in the course.

CONCLUSIONS

The interplays between anisotropy and strain localisation in granular soils were investigated using a hierarchical multiscale approach based on rigorous coupling of FEM and DEM, wherein clumped particles were used in the DEM part to simulate initial anisotropy. Biaxial compression tests

were simulated by the multiscale approach on samples under either smooth or rough boundary conditions. Key findings from the study are summarised as follows.

- (a) The bedding plane orientation is not necessarily the ‘weaker’ direction for the shear band to initiate. Either type-a or type-b shear bands can happen under smooth boundary conditions, which is consistent with the experimental observations by Tatsuoka *et al.* (1990). Under rough boundary conditions, cross-shaped double bands occur (type-a pairs with type-b), but they are not initiated simultaneously. The inception of the first band leads to increased resultant shear stress on the platen, while the later developing one offsets the shear stress towards zero at the residual state. Significant particle rotation is observed inside shear bands except at the intersection of the cross-shaped double bands, where vanishing average particle rotation is found.
- (b) Non-coaxial material responses may serve as an important direct (nominal) triggering mechanism for

strain localisation, while the fundamental (physical) triggering factors may vary greatly in a BVP for sand. For example, initial anisotropy, imperfection, inhomogeneity, boundary constraints and drainage condition can also cause non-coaxial material responses and induce strain localisation. Although non-coaxiality has long been investigated in the context of constitutive modelling of sand only, the present study is the first to discuss its direct correlation with strain localisation by evidence from multiscale analysis.

- (c) The two fabric anisotropy tensors ϕ_{ij}^c and ϕ_{ij}^p , defined by the distributions of the contact normals and the particle orientations, respectively, play different roles in triggering strain localisation. ϕ_{ij}^c begins to evolve immediately upon loading, while the evolution of ϕ_{ij}^p needs to be mobilised with larger shear and dilation. The asynchronous evolution of the two anisotropies can cause an initially coaxial packing to develop substantial non-coaxiality at small shearing levels to trigger strain localisation. The shearing strain level for ϕ_{ij}^p to reach the critical state is also much larger than that for ϕ_{ij}^c .
- (d) The final shear bands feature a high concentration of shear strain, large dilation and excessive particle rotations. Within the shear band, ϕ_{ij}^p attains an extremum (which can be either a minimum for an initially anisotropic specimen or a maximum for an initially random specimen). The local RVEs inside the shear band may attain critical state after shear with constant volume, constant stress and constant fabric anisotropies (in terms of both F_p and F_c), while those outside the shear band may experience mild deformation followed by unloading.

The current study constitutes a first step towards bridging the micromechanics of a granular soil and the macroscopic phenomena such as strain localisation. It is apparent that the micro- and meso-scale models considered in such an approach may influence the macroscopic responses and thus need careful calibrations to tackle specific problems. To account for inherent anisotropy, the observations and the conclusions drawn above have been based on a simple clump DEM model, which may be improved by using more complex particle shapes for better approximation of real sand particles (e.g. Mollon & Zhao, 2012, 2013, 2014). This multiscale investigation highlights the complicated nature of non-coaxiality, which may involve multiple influential factors such as particle orientation and contact normal distributions that jointly contribute to the anisotropic soil behaviour. This definitely deserves further theoretical consideration in the context of continuum soil mechanics.

ACKNOWLEDGEMENTS

The simulations were performed on a high-performance computing facility supported by the Science School Computational Science Initiative, HKUST. The study was financially supported by the Research Grants Council of Hong Kong through GRF 623211.

NOTATION

A_{cl}, I_{cl}	area, inertia of moment and density of a clump particle
D^{ep}	elasto-plastic modulus
D_{ijkl}	homogenised tangent modulus of a DEM packing
d^c, d_i^c	branch vector at a contact
$E(\theta)$	distribution function
e	local void ratio
f	FEM nodal force vector
f^c, f_i^c	contact force at a contact
K	FEM stiffness matrix

k_n, k_t	contact normal stiffness and tangential stiffness
N_p, N_c	particle number and contact number within a DEM packing
n^c, n_i^c	unit contact normal vector
n^p, n_i^p	unit particle orientation vector
p, q	mean effective stress and deviatoric stress
p_0, e_0	initial mean effective stress and void ratio prior to biaxial shear
r	radius of the constituent disc of a clump particle
r_{sq}	equivalent radius of a clump particle
r_{eq}	common radius of two contacting particles
t^c, t_i^c	unit tangential vector at a contact
u	FEM nodal displacement vector
$u_{i,j}$	FEM deformation field and boundary condition for local RVEs
V	total volume of a DEM packing
α	bedding plane angle of a RVE packing
β	non-coaxiality angle in a RVE element test
δ_{ij}	Kronecker delta
ϵ_1, ϵ_3	major and minor principal strain increment
ϵ_{ij}, e_{ij}	strain tensor and deviatoric strain tensor
ϵ_v, ϵ_q	volumetric strain and deviatoric strain
θ^p, θ	individual particle rotation and average particle rotation for a RVE F_{ij}^p packing
σ_1, σ_3	major and minor principal stress
σ_{ij}, s_{ij}	effective stress tensor and deviatoric stress tensor
$\phi_{ij}^c, F_{ij}^c, F_c$	contact normal based fabric tensor, deviatoric tensor and anisotropic intensity
$\phi_{ij}^p, F_{ij}^p, F_p$	particle orientation based fabric tensor, deviatoric tensor and anisotropic intensity
φ	interparticle friction angle
ω_{ij}	rigid body rotation of a RVE packing

REFERENCES

- Abelev, A. V. & Lade, P. V. (2003). Effects of cross anisotropy on three-dimensional behavior of sand. II: stress-strain behavior and shear banding. *J. Engng Mech. ASCE* **129**, No. 2, 160–166.
- Andrade, J. E. & Borja, R. I. (2006). Capturing strain localization in dense sands with random density. *Int. J. Numer. Methods Engng* **67**, No. 11, 1531–1564.
- Andrade, J. E., Baker, J. W. & Ellison, K. C. (2008). Random porosity fields and their influence on the stability of granular media. *Int. J. Numer. Analyt. Methods Geomech.* **32**, No. 10, 1147–1172.
- Andrade, J. E., Avila, C. F., Hall, S. A., Lenoir, N. & Viggiani, G. (2011). Multiscale modeling and characterization of granular matter: from grain kinematics to continuum mechanics. *J. Mech. Phys. Solids* **59**, No. 2, 237–250.
- Arthur, J. R. F. & Menzies, B. K. (1972). Inherent anisotropy in a sand. *Géotechnique* **22**, No. 1, 115–128, <http://dx.doi.org/10.1680/geot.1972.22.1.115>.
- Arthur, J. R. F., Chua, K. S. & Dunstan, T. (1977). Induced anisotropy in a sand. *Géotechnique* **27**, No. 1, 13–30, <http://dx.doi.org/10.1680/geot.1977.27.1.13>.
- Bardet, J. P. & Proubet, J. (1991). A numerical investigation of the structure of persistent shear bands in granular media. *Géotechnique* **41**, No. 4, 599–613, <http://dx.doi.org/10.1680/geot.1991.41.4.599>.
- Bauer, E., Huang, W. & Wu, W. (2004). Investigations of shear banding in an anisotropic hypoplastic material. *Int. J. Solids Structs* **41**, No. 21, 5903–5919.
- Bigoni, D. & Loret, B. (1999). Effects of elastic anisotropy on strain localization and flutter instability in plastic solids. *J. Mech. Phys. Solids* **47**, No. 7, 1409–1436.
- Casagrande, A. & Carillo, N. (1944). Shear failure of anisotropic materials. *J. Boston Soc. Civ. Engrs* **31**, No. 4, 74–87.
- Chang, C. S. & Hicher, P. Y. (2005). An elasto-plastic model for granular materials with microstructural consideration. *Int. J. Solids Structs* **42**, No. 14, 4258–4277.
- Chang, C. S. & Yin, Z.Y. (2010). Micromechanical modelling for inherent anisotropy in granular materials. *J. Engng Mech. ASCE* **136**, No. 7, 830–839.
- Chang, C. S., Yin, Z.Y. & Hicher, P. Y. (2011). Micromechanical analysis for inter-particle and assembly instability of sand. *J. Engng Mech. ASCE* **137**, No. 3, 155–168.

- Desrues, J. & Viggiani, G. (2004). Strain localization in sand: an overview of the experimental results obtained in Grenoble using stereophotogrammetry. *Int. J. Numer. Analyt. Methods Geomech.* **28**, No. 4, 279–321.
- Evans, T. M. & Frost, J. D. (2010). Multiscale investigation of shear bands in sand: physical and numerical experiments. *Int. J. Numer. Analyt. Methods Geomech.* **34**, No. 15, 1634–1650.
- Fu, P. & Dafalias, Y. F. (2011a). Fabric evolution within shear bands of granular materials and its relation to critical state theory. *Int. J. Numer. Analyt. Methods Geomech.* **35**, No. 18, 1918–1948.
- Fu, P. & Dafalias, Y. F. (2011b). Study of anisotropic shear strength of granular materials using DEM simulation. *Int. J. Numer. Analyt. Methods Geomech.* **35**, No. 10, 1098–1126.
- Gao, Z. & Zhao, J. (2013). Strain localization and fabric evolution in sand. *Int. J. Solids Structs* **50**, No. 22–23, 3634–3648.
- Gao, Z., Zhao, J., Li, X.S. & Dafalias, Y. F. (2014). A critical state sand plasticity model accounting for fabric evolution. *Int. J. Numer. Analyt. Methods Geomech.* **38**, No. 4, 370–390.
- Gross, L., Bourgoignie, L., Hale, A. J. & Mühlhaus, H.B. (2007). Interface modeling in incompressible media using level sets in Escrip. *Phys. Earth Planetary Interiors* **163**, No. 1–4, 23–34.
- Guo, N. & Zhao, J. (2013a). A hierarchical model for cross-scale simulation of granular media. *AIP Conf. Proc.* **1542**, 1222–1225.
- Guo, N. & Zhao, J. (2013b). The signature of shear-induced anisotropy in granular media. *Comput. Geotech.* **47**, 1–15.
- Guo, N. & Zhao, J. (2014). A coupled FEM/DEM approach for hierarchical multiscale modelling of granular media. *Int. J. Numer. Methods Engng* **99**, No. 11, 789–818.
- Gutierrez, M. & Ishihara, K. (2000). Non-coaxiality and energy dissipation in granular material. *Soils Found.* **40**, No. 2, 49–59.
- Hall, S. A., Bornert, M., Desrues, J., Pannier, Y., Lenoir, N., Viggiani, G. & Bésuelle, P. (2010). Discrete and continuum analysis of localised deformation in sand using X-ray μ CT and volumetric digital image correlation. *Géotechnique* **60**, No. 5, 315–322, <http://dx.doi.org/10.1680/geot.2010.60.5.315>.
- Hasan, A. & Alshibli, K. A. (2010). Experimental assessment of 3D particle-to-particle interaction within sheared sand using synchrotron microtomography. *Géotechnique* **60**, No. 5, 369–379, <http://dx.doi.org/10.1680/geot.2010.60.5.369>.
- Hicher, P. Y., Chang, C. S. & Dano, C. (2008). A multi-scale modeling of grouted sand. *Int. J. Solids Structs* **45**, No. 16, 4362–4374.
- Kruyt, N. & Rothenburg, L. (1998). Statistical theories for the elastic moduli of two-dimensional assemblies of granular materials. *Int. J. Engng Sci.* **36**, No. 10, 1127–1142.
- Lade, P. V. & Abelev, A. V. (2003). Effects of cross anisotropy on three-dimensional behavior of sand. II: volume change behavior and failure. *J. Engng Mech. ASCE* **129**, No. 2, 167–174.
- Lade, P. V., Nam, J. & Hong, W. P. (2008). Shear banding and cross-anisotropic behavior observed in laboratory sand tests with stress rotation. *Can. Geotech. J.* **45**, No. 1, 74–84.
- Li, X. & Yu, H.S. (2010). Numerical investigation of granular material behaviour under rotational shear. *Géotechnique* **60**, No. 5, 381–394, <http://dx.doi.org/10.1680/geot.2010.60.5.381>.
- Li, X. S. & Dafalias, Y. F. (2012). Anisotropic critical state theory: the role of fabric. *J. Engng Mech. ASCE* **138**, No. 3, 263–275.
- Luding, S. (2004). Micro-macro transition for anisotropic, frictional granular packings. *Int. J. Solids Structs* **41**, No. 21, 5821–5836.
- Meejun, N., Skeldon, A. C., Tüzün, U. & O’Sullivan, C. (2008). Wavelet analysis of DEM simulations of samples under biaxial compression. *Granular Matter* **10**, No. 5, 389–398.
- Miehe, C. & Dettmar, J. (2004). A framework for micro-macro transitions in periodic particle aggregates of granular materials. *Comput. Methods Appl. Mech. Engng* **193**, No. 3–5, 225–256.
- Miehe, C., Dettmar, J. & Zäh, D. (2010). Homogenization and two-scale simulations of granular materials for different micro-structural constraints. *Int. J. Numer. Methods Engng* **83**, No. 8–9, 1206–1236.
- Mokni, M. & Desrues, J. (1999). Strain localization measurements in undrained plane-strain biaxial tests on Hostun RF sand. *Mech. Cohesive-Frictional Mater.* **4**, No. 4, 419–441.
- Mollon, G. & Zhao, J. (2012). Fourier-Voronoi-based generation of realistic samples for discrete modelling of granular materials. *Granular Matter* **14**, No. 5, 621–638.
- Mollon, G. & Zhao, J. (2013). Generating realistic 3D sand particles using Fourier descriptors. *Granular Matter* **15**, No. 1, 95–108.
- Mollon, G. & Zhao, J. (2014). 3D generation of realistic granular samples based on random fields theory and fourier shape descriptors. *Comput. Methods Appl. Mech. Engng* **279**, 46–65.
- Mooney, M. A., Finno, R. J. & Viggiani, M. G. (1998). A unique critical state for sand? *J. Geotech. Geoenviron. Engng ASCE* **124**, No. 11, 1100–1108.
- Mühlhaus, H., Moresi, L., Gross, L. & Grotowski, J. (2010). The influence of non-coaxiality on shear banding in viscous-plastic materials. *Granular Matter* **12**, No. 3, 229–238.
- Nguyen, T. K., Combe, G., Caillerie, D. & Desrues, J. (2013). Modeling of cohesive granular materials by a multi-scale approach. *AIP Conf. Proc.* **1542**, 1194–1197.
- Nguyen, T. K., Combe, G., Caillerie, D. & Desrues, J. (2014). FEM \times DEM modelling of cohesive granular materials: numerical homogenization and multi-scale simulations. *Acta Geophysica* **62**, No. 5, 1109–1126.
- Nitka, M., Combe, G., Dascalu, C. & Desrues, J. (2011). Two-scale modeling of granular materials: a DEM-FEM approach. *Granular Matter* **13**, No. 3, 277–281.
- Oda, M. (1972a). Initial fabrics and their relations to mechanical properties of granular materials. *Soils Found.* **12**, No. 1, 17–36.
- Oda, M. (1972b). The mechanism of fabric changes during compressional deformation of sand. *Soils Found.* **12**, No. 2, 1–18.
- Oda, M. (1982). Fabric tensor for discontinuous geological materials. *Soils Found.* **22**, No. 4, 96–108.
- Rechenmacher, A. L. (2006). Grain-scale processes governing shear band initiation and evolution in sands. *J. Mech. Phys. Solids* **54**, No. 1, 22–45.
- Roscoe, K. H., Schofield, A. N. & Wroth, C. P. (1958). On the yielding of soils. *Géotechnique* **8**, No. 1, 22–53, <http://dx.doi.org/10.1680/geot.1958.8.1.22>.
- Rudnicki, J. W. & Rice, J. R. (1975). Conditions for the localization of deformation in pressure-sensitive dilatant materials. *J. Mech. Phys. Solids* **23**, No. 6, 371–394.
- Satake, M. (1982). Fabric tensor in granular materials. In *Deformation and failure of granular materials* (eds P. A. Vermeer and H. J. Luger), pp. 63–68. Rotterdam, the Netherlands: Balkema.
- Schofield, A. N. & Wroth, C. P. (1968). *Critical state soil mechanics*. London, UK: McGraw-Hill.
- Seyedi Hosseininia, E. (2012a). Discrete element modeling of inherently anisotropic granular assemblies with polygonal particles. *Particuology* **10**, No. 5, 542–552.
- Seyedi Hosseininia, E. (2012b). Investigating the micromechanical evolutions within inherently anisotropic granular materials using discrete element method. *Granular Matter* **14**, No. 4, 483–503.
- Šmilauer, V., Catalano, E., Chareyre, B., Dorofeenko, S., Duriez, J., Gladky, A., Kozicki, J., Modenese, C., Scholtès, L., Sibille, L., Stránský, J. & Thoeni, K. (2010). *Yade documentation*, 1st edn. See <https://www.yade-dem.org/doc/> (accessed 23/06/2015).
- Tatsuoka, F., Sakamoto, M., Kawamura, T. & Fukushima, S. (1986). Strength and deformation characteristics of sand in plane strain compression at extremely low pressures. *Soils Found.* **26**, No. 1, 65–85.
- Tatsuoka, F., Nakamura, S., Huang, C.C. & Tani, K. (1990). Strength anisotropy and shear band direction in plane strain tests of sand. *Soils Found.* **30**, No. 1, 35–54.
- Tejchman, J. & Górski, J. (2010). Finite element study of patterns of shear zones in granular bodies during plane strain compression. *Acta Geotechnica* **5**, No. 2, 95–112.
- Tejchman, J. & Wu, W. (2009). Non-coaxiality and stress-dilatancy rule in granular materials: FE investigation within micro-polar hypoplasticity. *Int. J. Numer. Analyt. Methods Geomech.* **33**, No. 1, 117–142.
- Vardoulakis, I. (1996). Deformation of water-saturated sand: I. Uniform undrained deformation and shear band. *Géotechnique* **46**, No. 3, 441–456, <http://dx.doi.org/10.1680/geot.1996.46.3.441>.

- Wong, R. K. S. & Arthur, J. R. F. (1985). Induced and inherent anisotropy in sand. *Géotechnique* **35**, No. 4, 471–481, <http://dx.doi.org/10.1680/geot.1985.35.4.471>.
- Wren, J. R. & Borja, R. I. (1997). Micromechanics of granular media Part II: overall tangential moduli and localization model for periodic assemblies of circular disks. *Comput. Methods Appl. Mech. Engng* **141**, No. 3–4, 221–246.
- Yu, H. S. & Yuan, X. (2006). On a class of non-coaxial plasticity models for granular soils. *Proc. R. Soc. A* **462**, No. 2067, 725–748.
- Zhao, J. & Guo, N. (2013). Unique critical state characteristics in granular media considering fabric anisotropy. *Géotechnique* **63**, No. 8, 695–704, <http://dx.doi.org/10.1680/geot.12.P040>.